Atmos. Meas. Tech., 6, 1855–1868, 2013
www.atmos-meas-tech.net/6/1855/2013/
doi:10.5194/amt-6-1855-2013
© Author(s) 2013. CC Attribution 3.0 License.

Atmospheric Measurement Techniques
Open Access

Retrieval of cirrus optical thickness and assessment of ice crystal shape from ground-based imaging spectrometry

M. Schäfer, E. Bierwirth, A. Ehrlich, F. Heyner, and M. Wendisch

Leipzig Institute for Meteorology, University of Leipzig, Leipzig, Germany

Correspondence to: M. Schäfer (michael.schaefer@uni-leipzig.de)

Received: 21 December 2012 – Published in Atmos. Meas. Tech. Discuss.: 4 February 2013
Revised: 25 June 2013 – Accepted: 25 June 2013 – Published: 1 August 2013

Abstract. A ground-based hyperspectral imaging spectrometer (AisaEAGLE, manufactured by Specim Ltd., Finland) is applied to measure downward spectral radiance fields with high spatial (1024 spatial pixels within 36.7° field of view), spectral (488 spectral pixels, 400–970 nm, 1.25 nm full width at half maximum), and temporal (4–30 Hz) resolution. The calibration, measurement and data evaluation procedures are introduced. A new method is presented to retrieve the cirrus optical thickness (τ_{ci}) using the spectral radiance data collected by AisaEAGLE. The data were collected during the Cloud Aerosol Radiation and tuRbulence of trade wInd cumuli over BArbados (CARRIBA) project in 2011. The spatial inhomogeneity of the investigated cirrus is characterised by the standard deviation of the retrieved τ_{ci} as well as the width of its frequency distribution. By comparing measured and simulated downward solar spectral radiance as a function of scattering angle, some evidence of the prevailing cirrus ice crystal shape can be obtained and subsequently used to substantiate the retrieval of τ_{ci}. The sensitivity of the retrieval method with respect to surface albedo, effective radius (r_{eff}), cloud height and ice crystal shape is quantified. An enhanced sensitivity of the retrieved τ_{ci} is found with respect to the surface albedo (up to 30 %) and ice crystal shape (up to 90 %). The sensitivity with regard to the effective ice crystal radius (≤ 5 %) and the cloud height (≤ 0.5 %) is rather small and can be neglected.

1 Introduction

Satellite-derived cirrus cloud climatology includes cloud cover, optical thickness and crystal effective radius. Changing either of those parameters may change the magnitude of their radiative forcing. For example, current global circulation models assume a standard value of 25 µm for the ice crystal effective radius. For slightly smaller crystals, cirrus clouds would have a stronger cooling effect (Garrett et al., 2003). Furthermore, cirrus clouds often show a high spatial and temporal variability and in addition might be optically thin. This makes it hard to detect cirrus by common remote sensing techniques. The microphysical composition adds a further complication. The crystal shape can change the cloud radiative properties substantially, which can cause biases in both satellite retrievals (based on reflected radiance, Eichler et al., 2009) and the energy budget estimates (related to irradiance, Wendisch et al., 2005, 2007).

Carlin et al. (2002) found a variability of cirrus albedo as derived from millimetre cloud radar datasets of up to 25 % due to the spatial cirrus inhomogeneity (over weakly reflecting surfaces and at high solar zenith angles). Therefore, vertical and horizontal cloud inhomogeneities are considered to be one of the most likely reasons for the disagreement between satellite cloud retrievals and in situ measurements. Varnai and Marshak (2001) have shown that optical thickness retrievals by e.g. MODIS (Moderate-Resolution Imaging Spectroradiometer) are biased mainly due to horizontal inhomogeneities and the related radiative smoothing (Marshak et al., 1995; Oreopoulos et al., 2000).

Passive satellite imaging spectroradiometers used for cloud retrievals measure the radiance field reflected by clouds. The applicability of those data for remote sensing is

limited by the aforementioned radiative smoothing and other 3-D effects, but also by the number of wavelength bands and spatial resolution of the sensor. A second source of uncertainty in cirrus retrievals arises from the forward simulation applied within the retrieval algorithm. In the special case of ice clouds, assumptions about the crystal shape and the corresponding scattering properties are made. Eichler et al. (2009) have shown that these assumptions can add an uncertainty of up to 70 % and 20 % in optical thickness and effective radius, respectively. For the determination of the ice crystal shape, McFarlane and Marchand (2008) developed a best-fit ice crystal scattering model that uses angular dependent measurements from coincident Multi-angle Imaging Spectroradiometer (MISR) and MODIS reflectances. Sensitivity to particle shape is provided by the multi-angle information from MISR. McFarlane and Marchand (2008) were therefore able to distinguish between ice crystal habits such as aggregates and plates.

One way to check the retrieval algorithms with respect to horizontal cloud heterogeneity, spatial resolution and crystal shape is provided by flying airborne versions of spectroradiometers above cirrus clouds, such as the MODIS Airborne Simulator (MAS). With extensive microphysical and solar radiation instruments as well as radiative transfer simulations, Schmidt et al. (2007) and Eichler et al. (2009) investigated the differences between retrieved and measured microphysical cloud properties. Schmidt et al. (2007) revealed large gaps between the retrieved effective radius from MAS and simultaneous in situ measurements. This disagreement has not been resolved yet, partly because it has been extremely difficult to collocate remote sensing above the clouds and concurrent in-cloud microphysical measurements. Such experiments are extremely important to link satellite cloud observations of coarse resolution to spatially highly resolved measurements of cloud properties. Unfortunately, such experiments are rare, partly because instruments like MAS are very complex and expensive and are not available for frequent cloud experiments.

Furthermore, there are only few cloud-resolving model studies on cirrus inhomogeneities. They investigate, for example, the radiative impact of the cirrus structure (Dobbie and Jonas, 2001), turbulence effects (Liu et al., 2003) or shear instabilities (Marsham and Dobbie, 2003). For a realistic simulation, a high spatial and temporal resolution is required to represent the small-scale features of cirrus inhomogeneities. In this regard, highly resolved measurements with ground-based imaging spectrometers can be a helpful tool to provide information on the cirrus inhomogeneities in terms of radiance and cirrus optical thickness.

In this study, a ground-based hyperspectral imaging spectrometer (AisaEAGLE, Hanus et al., 2008) is applied to measure downward spectral radiance fields with high spatial (1024 spatial pixels within 36.7° field of view, FOV), spectral (488 spectral pixels, 400–970 nm, 1.25 nm full width at half maximum, FWHM), and temporal (4–30 Hz) resolution. In Sect. 2, the AisaEAGLE is technically characterised, and its calibration and data evaluation procedures are described and exemplified. Section 3 introduces a new method to retrieve the cirrus optical thickness (τ_{ci}) from spectral radiance data, which also uses angular sampling of the phase function to obtain information about the particle shape. Its application to measurements is presented in Sect. 4. A sensitivity study regarding the input parameters for the retrieval algorithm is given in Sect. 5.

It needs to be mentioned that this study does not fully capitalise on the hyperspectral capabilities of AisaEAGLE. Here, only one wavelength (530 nm) is used. Thus, the paper is regarded to be a first feasibility study to show the potential of AisaEAGLE for ground-based measurements of downward solar spectral radiances and for retrievals of cloud microphysical properties like the cirrus optical thickness from the spectral measurements. In future studies, the wavelength range used for data evaluation will be extended to increase the number of retrieved cloud optical properties.

2 Measurements of spectral radiance fields

2.1 Campaign and measurement site

In April 2011, spectral measurements of downward solar radiance with the hyperspectral sensor AisaEAGLE were performed on Barbados during the second campaign of the Cloud Aerosol Radiation and tuRbulence of trade wInd cumuli over BArbados (CARRIBA) project (Siebert et al., 2012). The aim of CARRIBA was to investigate microphysical and radiative processes within and next to shallow trade wind cumuli by helicopter-borne and ground-based observations (e.g. Werner et al., 2013a,b). However, also cirrus clouds have frequently been observed by the ground-based instrumentation.

During the CARRIBA project in 2011, the hyperspectral sensor AisaEAGLE was located in the Barbados Cloud Observatory (BCO) of the Max Planck Institute for Meteorology (Hamburg, Germany) at Deebles Point (13.15° N, 59.42° W), a cape at the east coast of Barbados.

Additionally, measurements performed with a Raman lidar and a cloud radar as well as radiosonde data are available from the same site. A more detailed description of the BCO is provided by Siebert et al. (2012). In parallel to the AisaEAGLE radiance measurements, all-sky images were collected every 15 s to monitor the cloud situation (cloud coverage, cloud type, heading).

Downward spectral radiance was measured under inhomogeneous cloud cover on 14 different days. Each day, two hours of data were collected in parallel to the helicopter flights. While trade wind cumuli were not always present, cirrus clouds were observed during each measurement. In the following, four measurement cases are evaluated with only cirrus clouds to exclude any radiative effects by low cumuli.

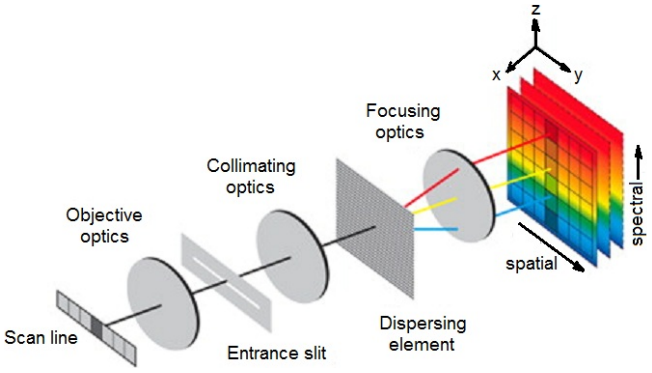

Fig. 1. Optical scheme of an imaging spectrometer. Adapted from DellEndice et al. (2009).

2.2 Hyperspectral imager AisaEAGLE

The AisaEAGLE is a commercial imaging spectrometer which is manufactured by Specim Ltd. in Finland (Hanus et al., 2008). It is a single-line sensor with 1024 spatial pixels. The instrument measures radiances in three dimensions: space, time and wavelength. The spatial and spectral dimensions are resolved by an optical assembly that displays the image onto a two-dimensional (2-D) sensor chip. The third dimension, time, corresponds to the motion of the clouds passing over the sensor. An optical schematic for the path of the electromagnetic radiation detected by the central spatial pixel is shown in Fig. 1.

The incoming solar radiation within the field of view (FOV) of AisaEAGLE is collected by a lens and an entrance slit. A collimating optics directs the radiation to a grating (dispersing element), where it is dispersed into its spectral components. The spectral components are focused on the detector, which consists of a charge-coupled device (CCD) element for the spatial and spectral dimensions.

In contrast to airborne measurements such as reported, for example, by Bierwirth et al. (2013), the 2-D image evolves from the cloud movement and not from the sensor movement. The sensor is aligned perpendicularly to the direction of the cloud movement, thus 2-D images of clouds with high spatial resolution are obtained. The FOV of the AisaEAGLE depends on the lens that is used for the measurements. During CARRIBA, a lens with an opening angle of about 36.7° was mounted. Figure 2 shows the size of a single image pixel and the swath of the entire image as a function of cloud height.

While the swath increases with distance to the cloud by the tangent of the opening angle, the pixel size depends on its position on the sensor line. The FOV of a pixel (the pixel width) in the centre (viewing zenith) is smaller than that of a pixel at the edge. For example, a cloud at an altitude of 10 000 m yields an average pixel size of 6.6 m (6.3 m–6.9 m) with 6 700 m swath. To obtain 2-D images, the temporal dimension of the hyperspectral measurements also translates to a spatial quantity: the length l_{pixel} of the FOV of a pixel is the product of the perpendicular cloud drifting velocity v_{cloud} and the selected integration time t_{int} for the measurement. Accounting for a non-perfect perpendicular orientation with the angle α between the flow direction of the cirrus and the orientation of the sensor line, l_{pixel} is then given by

$$l_{\mathrm{pixel}} = |\sin\alpha| \cdot v_{\mathrm{cloud}} \cdot t_{\mathrm{int}}. \quad (1)$$

Figure 3 illustrates the measurement geometry needed to derive the scattering angles ϑ for each spatial pixel. The scattering angle ϑ is calculated from the scalar product of the vector of the incoming solar radiation ($\boldsymbol{SC}$) and the vector of the radiation scattered into the sensor direction ($\boldsymbol{CD}$):

$$\cos\vartheta = \frac{\boldsymbol{CD}\cdot\boldsymbol{SC}}{|\boldsymbol{CD}|\cdot|\boldsymbol{SC}|} = \cos\varphi_0\cdot\sin\theta_0\cdot\sin\beta_{\mathrm{i}} + \cos\theta_0\cdot\cos\beta_{\mathrm{i}}. \quad (2)$$

θ_0 is the solar zenith angle and β_{i} is the viewing zenith angle of spatial pixel i. The solar azimuth angle φ is considered relative to the azimuth angle of the AisaEAGLE sensor line. Therefore, φ is cancelled out in Eq. (2).

For each spatial pixel the radiance is measured spectrally between 400 and 970 nm with 488 wavelength pixels. The spectral resolution is 1.25 nm full width at half maximum (FWHM). Since this spectral range covers more than one octave, the range from 800–970 nm requires order sorting. For this, AisaEAGLE has a second order depression using order blocking filters mounted near the detector. The integration time and the measurement rate are adjustable from 0.1 to 200 ms and 4 to 30 Hz. During CARRIBA a frame rate of 4 Hz was used. The integration time was chosen between 10 and 30 ms, depending on the illumination of the cloud scene.

2.3 Calibration, corrections and data handling

2.3.1 Calibration

The data collected by the AisaEAGLE are given in counts per integration time. A calibration to obtain radiances I in units of $\mathrm{W\,m^{-2}\,nm^{-1}\,sr^{-1}}$ is performed with an integrating sphere and the software AisaTools (provided by the manufacturer of AisaEAGLE). The dark current is determined separately with a shutter. The calibration factors for each pixel are calculated from the calibration measurements using a certified radiance standard (integrating sphere, uncertainty: ± 6 %) traceable to the US National Institute of Standards and Technology.

2.3.2 Smear correction

Since the AisaEAGLE detector is based on CCD technique, it is necessary to correct for the smear effect in calibration and measurement data. The smear effect occurs during the read-out process of the collected photoelectrons, which are shifted step by step from one spectral pixel to the neighbouring one into the direction of the read-out unit (Fig. 4). The read-out process is not infinitely fast. Due to the fact that

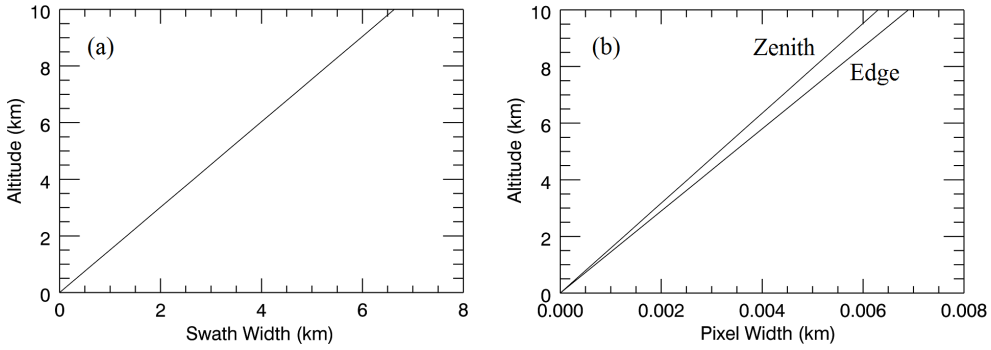

Fig. 2. Characteristic **(a)** swath and **(b)** pixel width for AisaEAGLE using the 36.7° lens.

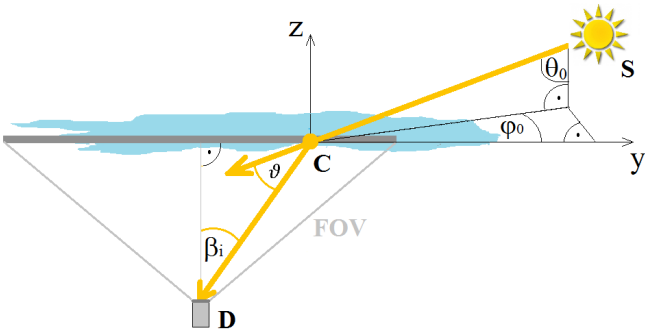

Fig. 3. Illustration of the AisaEAGLE measurement geometry in a Cartesian coordinate system (x, y, z) with position of the Sun (S), a scattering cloud particle (C) and the AisaEAGLE detector (D). θ_0 is the solar zenith angle, φ_0 the solar azimuth angle, ϑ the scattering angle, and β_i the viewing angle of the corresponding pixel.

radiation can still reach the sensor during the read-out, the pixels are contaminated by an additional signal. The read-out process begins at the red end of the spectral range. Therefore, the additional signal (smear effect) is larger for shorter wavelengths, because the corresponding charges have to traverse the entire chip.

The measurements can be corrected for the smear effect by applying the correction algorithm:

$$
\begin{aligned}
&x_1 = y_1,\\
&x_2 - S_c \cdot y_1 = y_2,\\
&x_3 - S_c \cdot (y_1 + y_2) = y_3,\\
&\cdots,\\
&x_n - S_c \cdot (\Sigma_{i=1}^{n} y_{i-1}) = y_n,
\end{aligned}
\qquad (3)
$$

where x_i are the uncorrected and y_i are the corrected digital counts with the wavelength index $i = 1,\ldots,n$. The smear correction factor $S_c = t_{\text{read-out}} / t_{\text{int}}$ is the ratio of the duration of a read-out step to the total integration time. For the first read-out step no correction is necessary, since the counts from the first pixel are shifted directly into the read-out unit. During the whole read-out process, the illumination of all pixels is assumed to remain constant. Therefore, new charges are still generated while the original charges are already shifted towards the read-out unit. The original charge from a given pixel therefore increases by the radiation that falls on the pixel the charge travels through. The increase is proportional to the smear correction factor S_c as well as the illumination of the pixels (see the fourth line of Fig. 4).

The smear effect must be taken into account for each measurement as well as for the calibration. It should be mentioned that the AisaEAGLE CCD element consists of 1024 spectral pixels for the hypothetic wavelength range from 100 to 1300 nm. However, due to the optical assembly, the effective spectral range of AisaEAGLE is decreased to 502 pixels in the range of 400 to 970 nm (so-called effective wavelength range). Spectral pixels below or above this range receive stray light from pixels within the effective wavelength range. This makes those pixels useless for data evaluation. Tests have shown that during atmospheric measurements the signal outside the effective wavelength range can be neglected for the smear correction (which significantly reduces the required data storage space). This is because solar spectral radiance is typically larger for shorter (400 nm) than for longer (900 nm) wavelengths.

Unfortunately, this does not hold for the calibration. The halogen calibration lamp of the integrating sphere is much colder than the Sun and emits radiation with a maximum in the near-infrared range (1000 nm) and low values at shorter wavelength (400 nm). Consequently, the out-of-range wavelength pixels above 1000 nm receive a significant amount of radiation.

A comparison between calibration coefficients derived with and without including the out-of-range pixels is shown in Fig. 5. Significant differences are observed for wavelengths below 500 nm, which agrees with the theory of the smear effect. Differences range from 3 % at 970 nm wavelength to 13 % at 400 nm wavelength. Therefore, it is necessary to use the entire AisaEAGLE spectral range during calibration, even though it is not used during data evaluation.

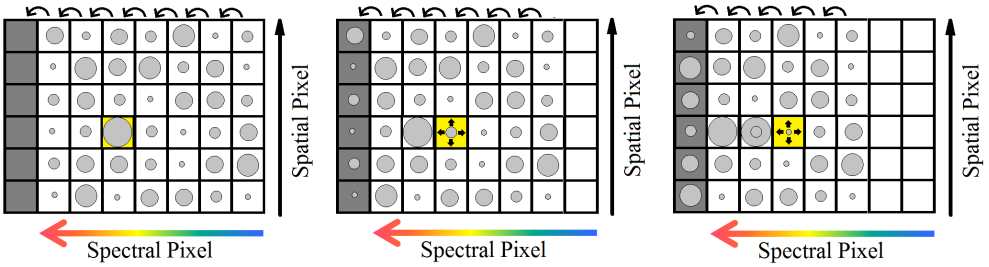

Fig. 4. Illustration of the read-out process and the smear effect. The grey bar on the left side illustrates the read-out unit. The arrows indicate the shifting direction of the photo-electrons. The magnitude of the signal of each pixel is indicated by the size of the circles. The smear effect is illustrated for one spatial pixel which is exposed to additional illumination at one spectral pixel (yellow) during the read-out process.

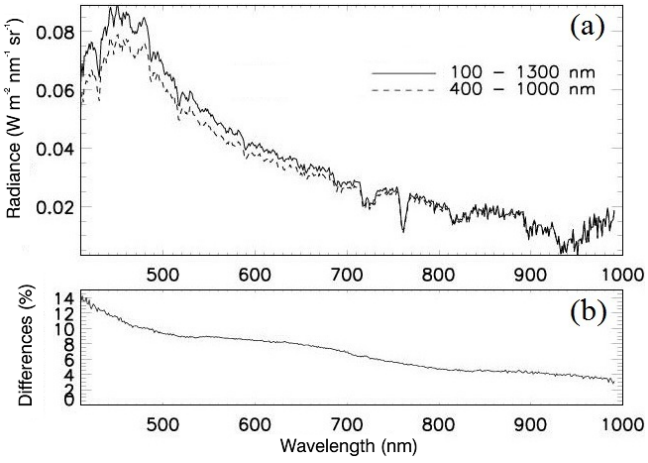

Fig. 5. (a) Spectral radiance measured with AisaEAGLE, for smear corrections considering different wavelength intervals in the calibration: 100–1300 nm (solid line), 400–1000 nm (dashed line). **(b)** Differences between the spectral radiances shown in panel **(a)**.

3 Retrieval of cirrus optical thickness

For the retrieval of cirrus optical thickness (τ_{ci}) from the measured downward spectral radiance $I^{\downarrow}$ transmitted through the cirrus, radiative transfer calculations were performed. The radiative transfer solver DISORT 2 (Discrete Ordinate Radiative Transfer) was applied. Input parameters such as cloud optical properties, aerosol content and spectral surface albedo are provided by the library for radiative transfer calculations (libRadtran, Mayer and Kylling, 2005). The so-called HEY (Hong, Emde, Yang) parametrisation was used to describe the scattering properties of ice crystals. It uses pre-calculated ice cloud optical properties including full phase matrices generated with the models by Yang et al. (2000).

In a first feasibility study, the simulations were performed only at a wavelength of 530 nm. This wavelength was chosen to match that of the lidar measurements at BCO. Since the BCO is located at the far end of this cape, the measurement site is surrounded by water, rocks and grass. For simplification the surface albedo in the radiative transfer simulations was assumed to be only water, as derived by Wendisch et al. (2004), providing a value of 0.068. libRadtran provides calculated Mie tables for rural, maritime, urban and tropospheric aerosol size distributions given in Shettle (1989). Because the measurements were performed in the vicinity of the coast, the maritime aerosol type was chosen. The cloud altitude and vertical extent was determined by lidar measurements at BCO. For the simulations, a fixed r_{eff} has to be defined as no direct retrieval from AisaEAGLE is possible. For this, a value of 20 µm was assumed. The assumed r_{eff} was taken from MODIS data collection 5 as best estimate for the area close to BCO. The value for the ice water content (IWC) is provided by libRadtran (Mayer and Kylling, 2005). libRadtran adapts the IWC with respect to the prescribed r_{eff} and simulated τ_{ci}. Therefore, a direct retrieval of the IWC is not possible, because our method is not sensitive to r_{eff}.

Using these input parameters, downward solar radiance $I^{\downarrow}_{cal}$ was simulated as a function of values of τ_{ci}. The simulations were performed for the whole FOV of AisaEAGLE and interpolated over the entire period of each measurement. Thus, a simulated grid of possible radiances and corresponding τ_{ci} is available for each time stamp of the measurement and each spatial pixel. The retrieved τ_{ci} is derived by interpolating the simulated radiances to the measured value for each spatial pixel using a linear interpolation. To handle the ambiguity of the simulations, only cloud optical thickness smaller than the one corresponding to the maximum radiance was considered. The uncertainty caused by using a fixed r_{eff}, surface albedo, cloud height and crystal shape is analysed in a sensitivity study in Sect. 5.

The imaging measurements require an accurate description of the sensor geometry in the simulations as shown in Fig. 3. The sensor was aligned horizontally. The sensor azimuth angle was not measured directly but estimated from measurements during the time when the Sun's azimuthal position was in the direction of the sensor line. If both azimuth angles are equal, the measurements will be overexposed with a distinct maximum. The sensor azimuth angle can be derived from the time of that maximum. The viewing zenith

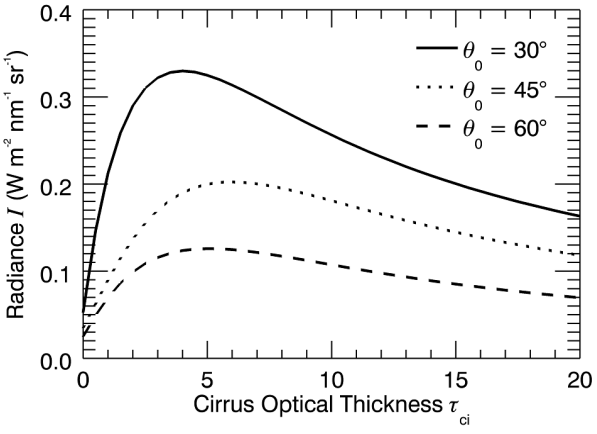

Fig. 6. Simulated radiance at 530 nm as a function of cloud optical thickness.

angle is given by the sensor FOV, which is $\beta = \pm 18°$. Related to this range, the downward solar radiance $I^{\downarrow}_{\mathrm{cal}}$ was calculated for angles with 0.3° steps.

Figure 6 shows radiance simulations for the solar zenith angles of 30, 45, and 60°, a solar azimuth angle of 90° and a cirrus with ice crystals in the shape of solid columns. The base of the cirrus is at 11 km altitude.

Figure 6 indicates that the retrieval of τ_{ci} is ambiguous: for example, at $\theta_0 = 30°$ a radiance of 0.2 W m^{-2} nm^{-1} sr^{-1} corresponds to τ_{ci} of either 1 or 15. This ambiguity has to be considered using additional information of the estimated τ_{ci}. In the case of thin cirrus (τ_{ci} less than about 3–4), the retrieval curve for low values of τ_{ci} must be used, for optically thicker cirrus the section for large τ_{ci} must be applied. Thus, independent knowledge of the expected range of τ_{ci} is important to avoid the ambiguity in the retrieval. During CARRIBA, this supplementary information was provided by all-sky images and lidar measurements. The all-sky images do not give a quantitative value of τ_{ci}, but they were evaluated qualitatively. An experienced observer is able to judge whether a given cloud has an optical thickness higher or lower than the maximum indicated in Fig. 6. All retrieved τ_{ci} presented within this study are in the range left of the maximum.

4 Measurements

4.1 Measurement cases

Four datasets from the CARRIBA project from different days were evaluated: 9, 16, 18 and 23 April 2011. These days showed persistent cirrus with no other clouds below. An overview of the main characteristics of the evaluated measurement periods can be found in Table 1.

Figure 7a to d show all-sky images from the beginning of the four cases. Within each image, the red arrow indicates the movement of the cirrus during the analysed period. The heading was derived by comparing the position of clouds in the sequence of all-sky images (15 s time resolution). The blue box indicates the area covered by the AisaEAGLE radiance measurements, i.e. the area of cirrus which is heading across the sensor line during the measurement period. Due to the fact that the AisaEAGLE was not orientated perfectly in perpendicular direction of the cirrus heading, the covered area is not a rectangle in most cases.

During all four measurement cases, τ_{ci} is estimated to be less than 3–4. That means that the ambiguity of Fig. 6 is avoided in all four cases. The cirrus field on 16 and 18 April was more homogeneous than that observed on 9 and 23 April. On 23 April, a 22° halo was identified on the all-sky images but unfortunately was not covered by the FOV of AisaEAGLE.

Fields of transmitted downward radiance $I^{\downarrow}$ as measured by AisaEAGLE for the four cases are presented in Fig. 8. The radiance is given for 530 nm in two-dimensional colour-scale images for all 1024 spatial pixels on the abscissa and the time of measurement on the ordinate.

The cloud structure seen in the all-sky images in Fig. 7a to d is clearly imprinted in the radiance field. The average values $\bar{I}^{\downarrow}$ of the measured radiance $I^{\downarrow}$ are given in Table 1. The highest value of $\bar{I}^{\downarrow}$ was observed on 23 April 2011 and the lowest on 9 April 2011.

Especially for 18 April 2011 it is evident that the image gets brighter from the left to the right side. During this day the sensor line of AisaEAGLE was orientated from north-west (pixel 1) to south-east (pixel 1024) while the Sun was in the East at the same time. This brightening is caused by enhanced scattering for small scattering angles, corresponding to the shape of the scattering phase function of ice crystals (see Fig. 9). Therefore, the radiative transfer calculations to retrieve τ_{ci} need to take into account the exact alignment of the sensor line and the exact position of the Sun. If the sensor orientation is carefully considered, the retrieval will account for this brightness effect caused by enhanced forward scattering by ice crystals.

Using the calculated scattering angles derived for each spatial pixel from Eq. (2), Fig. 8 can be displayed as a function of scattering angle as shown in Fig. 10. The scattering angles are symmetrical for each pixel to the pixel closest to the Sun. If the Sun's azimuthal position is almost perpendicular to the sensor line, a minimum appears in the detected scattering angles per spatial pixel. In such cases, the plot of $I^{\downarrow}$ as a function of the scattering angle would have overlapping sections. For clarity, one of those sections is assigned a negative sign in Fig. 8. Note that the images are not rectangular due to the movement of the Sun during the measurement period. The advantage of the illustration using scattering angles is that structures in the image related to the scattering phase function of the ice crystals now occur in a fixed position throughout the time series, as can be seen for 18 April 2011. The radiance always increases with decreasing scattering angle, which is a typical characteristic of the forward scattering by ice crystals.

Table 1. Characteristics of the evaluated measurement periods.

	9 April	16 April	18 April	23 April
start time (UTC)	13:26	13:43	13:43	16:45
average θ_0 (°)	36.7	28.6	28.5	14.5
cirrus flow direction	SW → NW	NW → SW	WSW → ESE	SSW → NNE
appearance	inhomogeneous	homogeneous	homogeneous	inhomogeneous
cloud height (km)	11–15	12–15	13–15	11–14
$\bar{I}^{\downarrow}$ (W m^{-2} nm^{-1} sr^{-1}) $\pm\sigma$	0.08 ± 0.02	0.11 ± 0.02	0.10 ± 0.03	0.16 ± 0.03
$\bar{\tau}_{\mathrm{ci}}$ $\pm\sigma$	0.41 ± 0.17	0.28 ± 0.09	0.20 ± 0.03	0.05 ± 0.04
covered ϑ range (°)	35.1–47.1	32.6–37.9	21.2–48.2	12.2–36.3

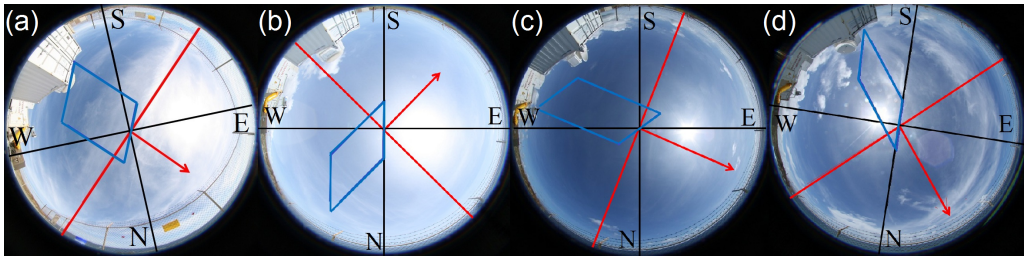

Fig. 7. All-sky images from the beginning of the evaluated AisaEAGLE radiance measurements for **(a)** 9 April, **(b)** 16 April, **(c)** 18 April and **(d)** 23 April 2011 with the flow direction of the cirrus (red arrow) and FOV of the AisaEAGLE radiance measurements (blue). Orientation given by black lines and capital letters.

4.2 Retrieved ice crystal shape

The ice crystal shape can be estimated from the directional distribution of radiance, considering the scattering phase function of different ice crystals. The all-sky images in Fig. 7 can be used as a first indicator. While on 9, 16 and 18 April no halo was visible, the 22 ° halo was observed on 23 April. Thus, regular ice crystals like columns or plates must have been present on that day. For the first three cases, irregular ice crystals are more likely, because the crystals did not produce a halo. The directional scattering features were analysed in detail with the AisaEAGLE measurements. Figure 11 shows the average measured downward solar radiance $I^{\downarrow}$ and its standard deviation as a function of the scattering angle for 18 April 2011. The standard deviation depends on the scattering angle and was calculated in intervals of $\Delta\vartheta = 0.3°$. Additionally, Fig. 11 includes simulations of downward solar radiance for different values of τ_{ci} and different ice crystal shapes. Figure 11a shows that for simulations assuming rough aggregates, no halo appears in the calculated radiance. However, for calculations with solid columns, plates as well as a mixture of ice crystals, the two halo regions are well defined in the simulation results. Furthermore, the best agreement between simulated and measured downward radiance $I^{\downarrow}$ was found for rough aggregates. For this reason, the τ_{ci} for 18 April 2011 was retrieved by assuming rough aggregates for the ice crystal shape in Sect. 4.3.

A similar analysis for 23 April 2011 is presented in Fig. 12. Enhanced radiance is measured at scattering angles between 20 and 26 °, which indicates the presence of a 22 ° halo. The halo is quite hard to identify in Fig. 10 due to the cirrus inhomogeneities and because the halo is quite weak. The averaged radiance displayed in Fig. 12 confirms this. The halo can be seen in the averaged data. However, due to the low τ_{ci} of 0.2, the maximum of the enhanced radiance within the halo region is relatively low. Concerning the ice crystal shape, best agreement is found for a mixture of different ice crystal shapes, while for aggregates the mismatch of the halo is obvious. A retrieval of the ice crystal shape is difficult because the cirrus was very inhomogeneous, as indicated by the high standard deviation. The variability of the radiances is about ± 0.03 W m^{-2} nm^{-1} sr^{-1}, which corresponds to a deviation of 20 % to the mean value. Therefore, the radiance fluctuations cannot be related to the scattering phase function. Considering that the analysed sequence on 23 April is short, with only about 6 minutes duration, it is more likely that changes of τ_{ci} account for the structure in the radiance. Therefore, in the following retrieval of the τ_{ci} for 23 April 2011, ice crystals in the shape of solid columns (default setting in libRadtran) were assumed.

For 9 and 16 April 2011 the retrieval of the ice crystal shape within the cirrus was not possible. Due to the geometry (wind direction, sensor alignment, solar position), only a narrow range of scattering angles was observed and the clouds were too inhomogeneous. The detected scattering angles just cover the edge of the halo regions. Therefore, the radiative transfer calculations to retrieve the τ_{ci} in Sect. 4.3 were performed for solid columns. An estimate of uncertainties related to the shape assumption is provided in Sect. 5.

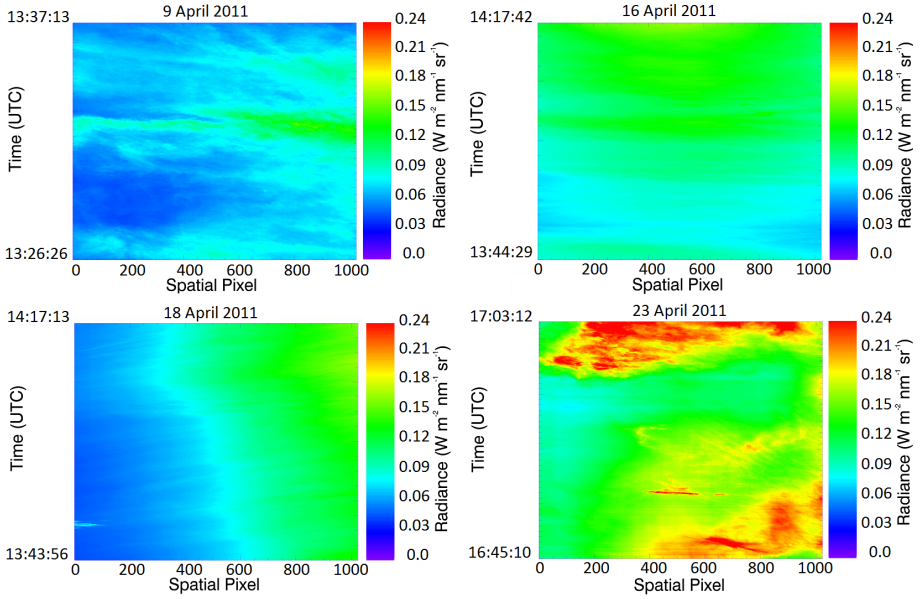

Fig. 8. Two-dimensional images of the evaluated AisaEAGLE radiance measurements at 530 nm with the measured $I^{\downarrow}$ (W m^{-2} nm^{-1} sr^{-1}) given in colour scales.

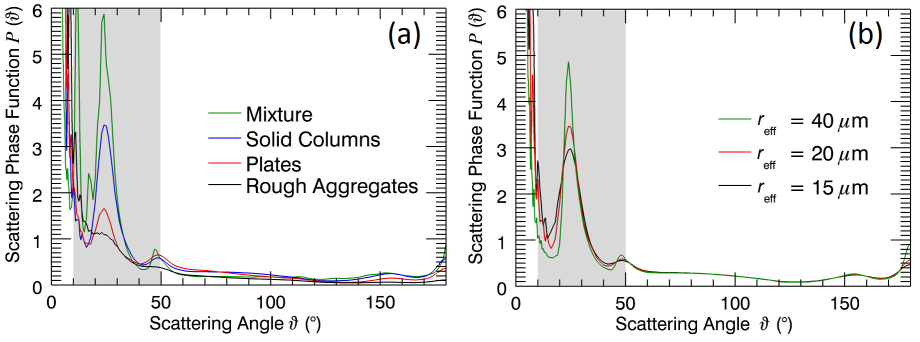

Fig. 9. Scattering phase functions for **(a)** the different ice crystal shapes at 20 µm and **(b)** solid columns, calculated for the three effective radii for the retrieval in this study. The grey bar indicates the captured scattering angle range during the measurements.

4.3 Retrieved cirrus optical thickness

The τ_{ci} retrieved by the presented method are displayed in Fig. 13. The measurement time and the pixel number have been converted into the cloud travel path and the swath width, respectively. For this, the altitude of the cloud base was used to derive the values for the abscissa. The average wind velocity in the same altitude, derived from the HYbrid Single-Particle Lagrangian Integrated Trajectory (HYSPLIT) model provided by the Air Resources Laboratory (ARL) of the US National Oceanic and Atmospheric Administration (NOAA), was used to convert the ordinate into a distance.

For 18 April 2011 the retrieved τ_{ci} indicates that the cloud is very homogeneous. This confirms that the observed increase in radiance (Figs. 8 and 10) results from enhanced forward scattering of ice crystals and has been considered correctly by the model. For 23 April 2011 quite inhomogeneous cirrus was observed with large areas of clear-sky regions in between.

Frequency distributions of the retrieved τ_{ci} for each measurement day are shown in Fig. 14. The histograms are normalised by the total of the retrieved τ_{ci} with a bin size of 0.01 in τ_{ci}. The average and the standard deviation of the retrieved τ_{ci} for each dataset are additionally listed in Table 1. High standard deviations compared to the average values are a further measure for the heterogeneity of the detected cloud situation. Thus, the AisaEAGLE measurements confirm that the cirrus on 16 and 18 April 2011 was more homogeneous than on 9 and 23 April 2011.

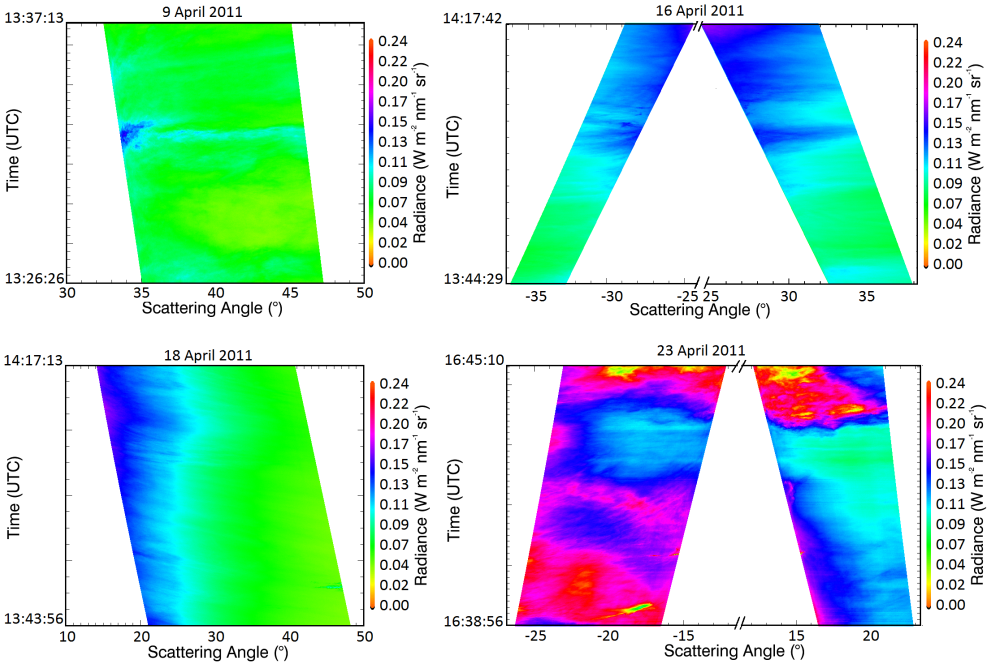

Fig. 10. Time series of the measured downward solar radiance $I^{\downarrow}$ during the four measurement cases as a function of scattering angle for each spatial pixel. The range of the abscissa of each image is fitted to the corresponding range of covered scattering angles.

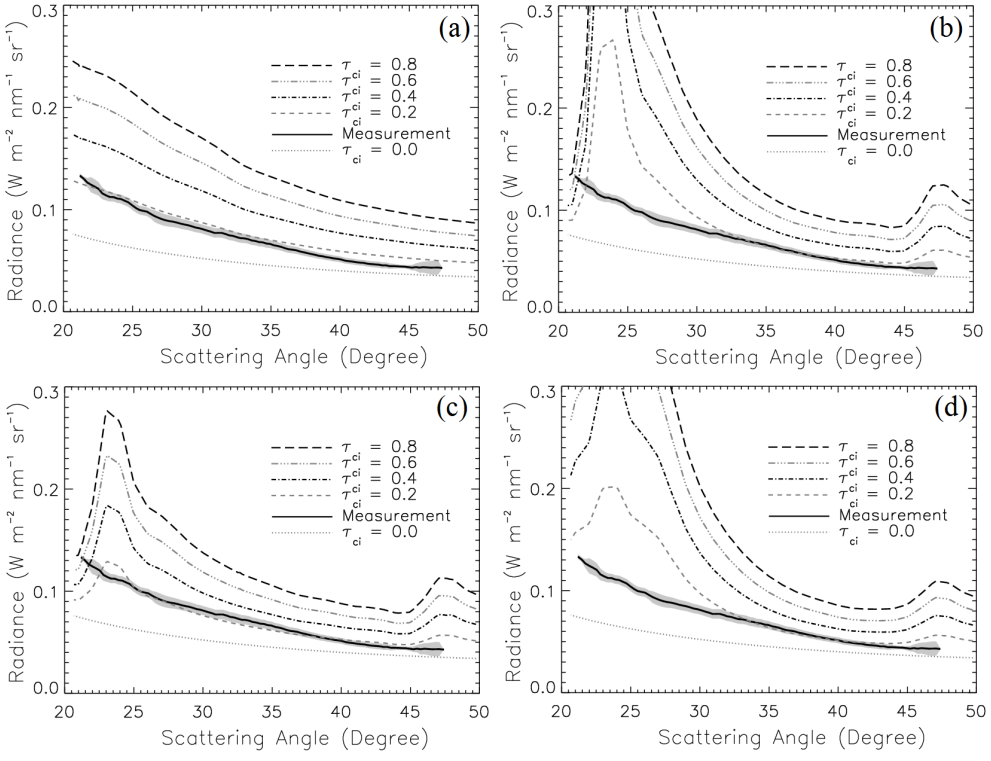

Fig. 11. Measured and simulated $I^{\downarrow}$ as a function of scattering angles. The standard deviation of the measurement is represented by the grey shade. Measurement from 18 April 2011. The simulations were performed for different τ_{ci} and an assumed ice crystal shape of **(a)** rough aggregates, **(b)** solid columns, **(c)** plates, and **(d)** mixture.

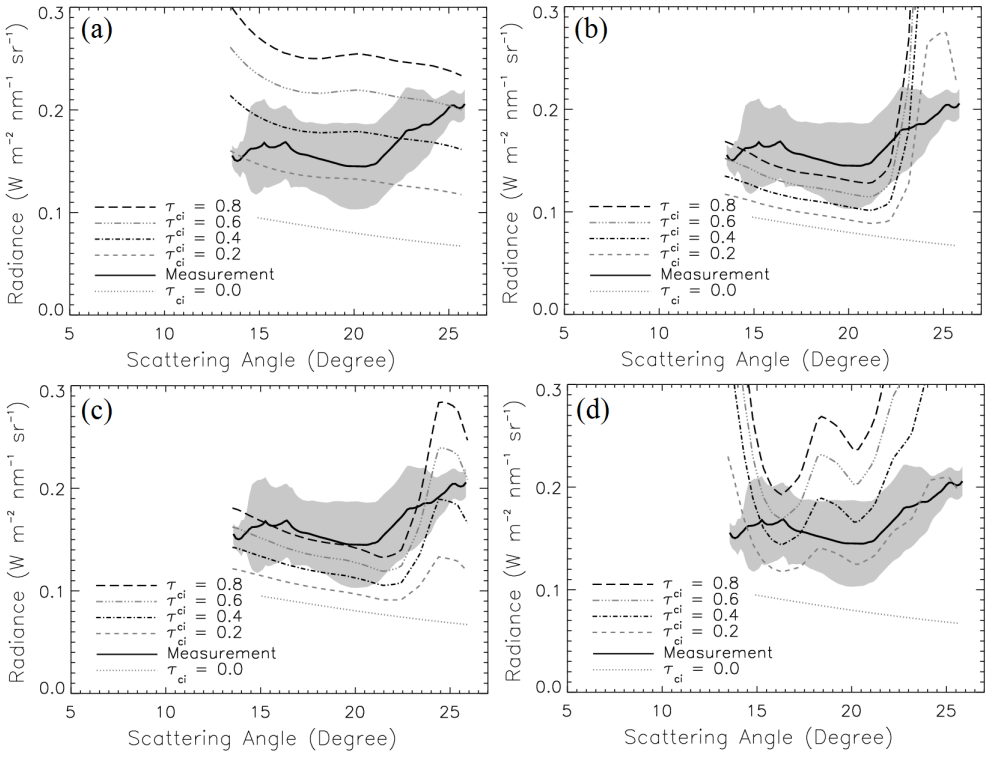

Fig. 12. Measured and simulated $I^{\downarrow}$ as a function of scattering angles. The standard deviation of the measurement is represented by the grey shade. Measurement from 23 April 2011. The simulations were performed for different τ_{ci} and an assumed ice crystal shape of **(a)** rough aggregates, **(b)** solid columns, **(c)** plates, and **(d)** mixture.

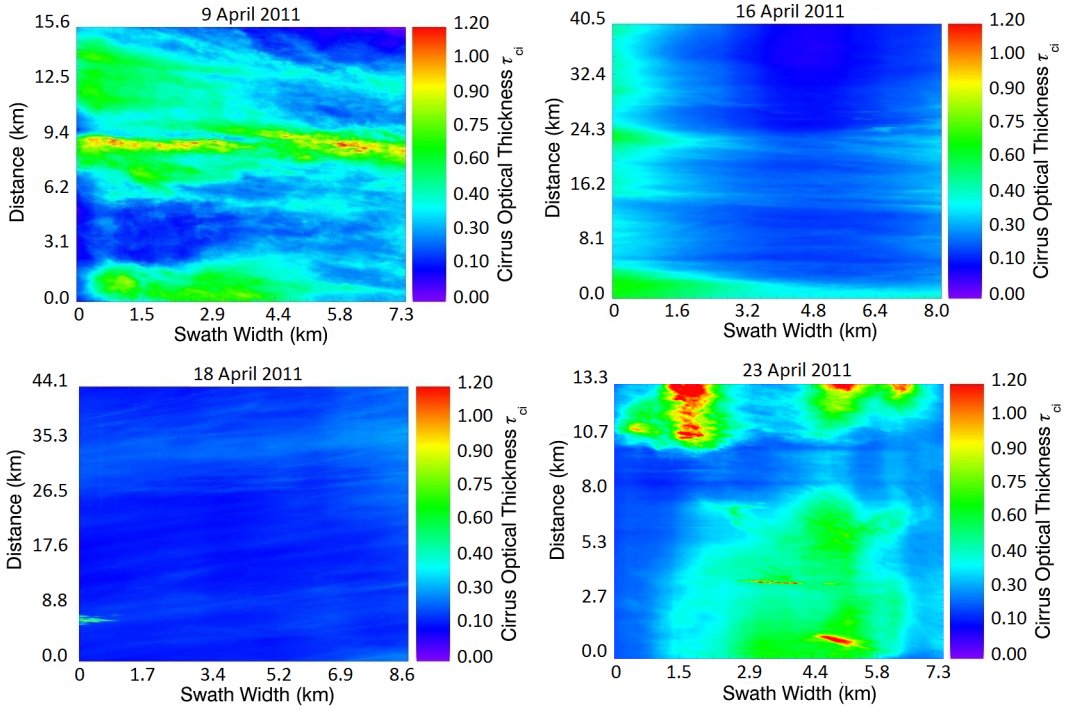

Fig. 13. Time series of the retrieved τ_{ci} during the four measurement cases for each spatial pixel. Abscissa and ordinate values are different due to different measurement conditions.

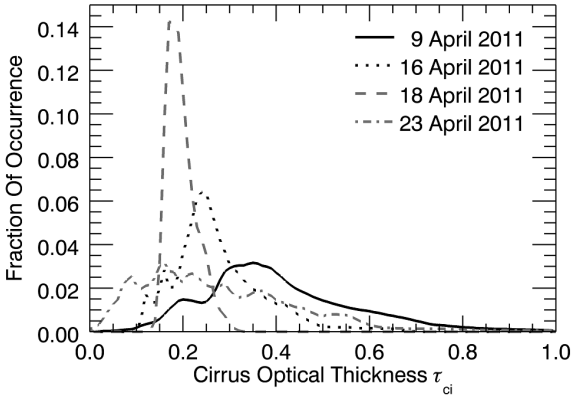

Fig. 14. Normalised histograms of τ_{ci} for each of the four considered measurement days. The bin size is 0.01 units of cirrus optical thickness τ_{ci}.

5 Sensitivity study

A sensitivity study has been performed to quantify the retrieval uncertainties with regard to the assumptions made on the model input parameters. We considered surface albedo, cloud properties such as the effective radius (r_{eff}) of the cirrus ice crystals, the cloud height and vertical extent, as well as the ice crystal shape.

For the sensitivity study all input parameters of the benchmark retrieval (BM; surface albedo: water, r_{eff}: 20 µm, cloud base: as derived by lidar for each case, ice crystal shape: solid columns) except one were kept constant. The sensitivity is expressed as the relative difference between the results of the sensitivity study, calculated using the average values of τ_{ci} (indicated by $\bar{\tau}_{ci}$). The results are listed in Table 2.

$$\Delta\bar{\tau}_{ci} = 100\,\% \cdot \left(\frac{\bar{\tau}_{ci,BM} - \bar{\tau}_{ci}}{\bar{\tau}_{ci,BM}} \right) \quad (4)$$

The benchmark case used a surface albedo of water (0.068 at 530 nm wavelength). Due to the fact that AisaEAGLE was not surrounded by water only, but also by grass and sand, possible uncertainties may occur in the retrieval results. To quantify those uncertainties the retrieval was repeated using the surface albedo for grass and sand (0.073 and 0.314) (Feister and Grewe, 1995). The effective radius r_{eff} was assumed to be 20 µm in the benchmark retrieval. The sensitivity study was performed for 15 and 40 µm. This range was estimated from MODIS measurements. The cirrus optical thickness τ_{ci} was too low to be detectable by MODIS during the period of the presented measurements. Therefore, the surrounding regions of Barbados were used to derive the range of the effective radii.

Another source for uncertainties is the cloud height and vertical extent. For the sensitivity tests the cloud was lifted 4 km upward and 4 km downward; the cloud vertical extent was not changed.

For ground-based measurements and without in situ observations it is impossible to directly determine the ice crystal shape within the cirrus. While solid columns were assumed in the benchmark retrieval, the sensitivity study was performed with plates and rough aggregates.

The differences between the benchmark retrieval and the sensitivity study vary in a range from less than one percent up to almost 90 % dependent on the input parameters. While Table 2 gives the different averages over the entire scene, Fig. 15 shows the uncertainties based on pure simulations. Radiances were simulated for τ_{ci} ranging from 0 to 0.5 and variable surface albedo, r_{eff}, cloud altitude and crystal shape. The simulated radiances are then applied to the retrieval method where the benchmark properties are assumed. Figure 9 shows the corresponding scattering phase functions for the assumed ice crystal shapes and in the special case of solid columns the scattering phase functions calculated for the three considered values of r_{eff}.

Table 2 shows that for a surface albedo higher than the benchmark value, τ_{ci} will be overestimated. For a grass surface with a slightly higher albedo than for water (0.073 compared to 0.068 of water), the overestimation is still small. The calculations assuming a sand surface albedo (0.378) show a strong overestimation of τ_{ci}. With a maximum of almost 29 % on 18 April 2011 and a minimum of around 12 % on 23 April 2011, the uncertainties are larger than those resulting from the measurement uncertainty. This indicates that the surface type has to be chosen correctly to enable accurate retrievals of τ_{ci}. This relation is confirmed in Fig. 15a. The retrieved τ_{ci} for the synthetic radiance above water and grass are almost identical. Compared to this, the retrieval curve for assuming a sand surface albedo shows higher values. The overestimation of up to 30 % seems to be relatively high; e.g. for very small τ_{ci} the percental difference can be quite large. However, looking at the retrieved τ_{ci} for the sensitivity study in Fig. 15a and the absolute values in Table 2, the difference in τ_{ci} is just about ± 0.1 and lower. This sensitivity study represents an extreme case, as the grass at Deebles Point was patchy and rather dry, so the literature estimate for the sand surface albedo is on the high side.

The downward solar radiance $I^{\downarrow}$ depends approximately linearly on the r_{eff} of the ice crystals. For the investigated cases it can be seen that for a smaller r_{eff} the retrieved τ_{ci} will be underestimated. For a larger r_{eff} the retrieved τ_{ci} will be overestimated. Looking at the differences listed in Table 2, linearity can be assumed. The absolute difference of $r_{eff} = 40$ µm, referring to $r_{eff} = 20$ µm, is four times higher than for $r_{eff} = 15$ µm referring to $r_{eff} = 20$ µm. This ratio approximately corresponds to the calculated differences in Table 2. However, comparing the results given in Table 2 and the retrieval curve shown in Fig. 15b, the differences are in a range below 5 %. This can also be seen in the non-significant change in the absolute values. Therefore, the uncertainty caused by estimating the unknown value of r_{eff} can be neglected. Comparing the scattering phase functions in

Table 2. Relative (%) and absolute difference of retrieved τ_{Ci} in comparison to benchmark case.

	9 April		16 April		18 April		23 April	
	rel.	abs.	rel.	abs.	rel.	abs.	rel.	abs.
surface albedo (grass)	2.6	0.01	0.4	0.00	0.6	0.00	0.25	0.00
surface albedo (sand)	27.8	0.11	20.6	0.06	28.9	0.06	11.51	0.01
r_{eff} (15 µm)	0.5	0.00	1.1	0.00	0.5	0.00	−0.54	−0.00
r_{eff} (40 µm)	−4.9	−0.02	−3.9	−0.01	−0.9	−0.00	−0.06	−0.00
cloud height (lower)	−0.45	−0.00	−0.28	−0.00	−0.14	−0.00	−0.06	−0.00
cloud height (higher)	0.31	0.00	0.19	0.00	−0.05	0.00	0.05	0.00
crystal shape (plates)	14.80	0.06	75.3	0.21	85.6	0.17	12.26	0.01
crystal shape (r. aggr.)	23.3	0.09	26.1	0.07	33.1	0.07	17.11	0.01

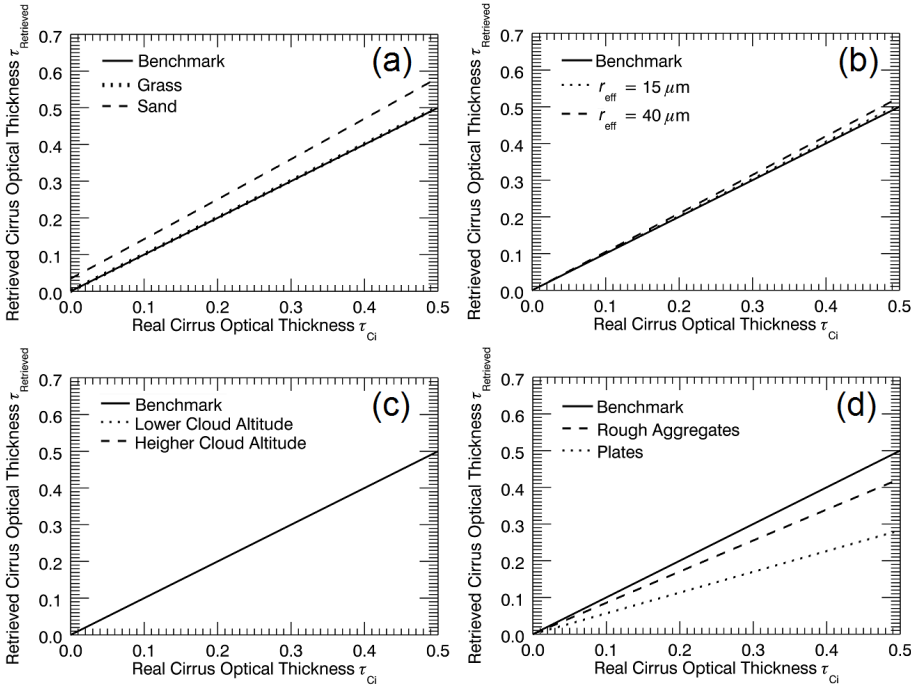

Fig. 15. Retrieval curves for the explanation of the sensitivity results concerning the **(a)** surface albedo, **(b)** effective radius, **(c)** cloud height, and **(d)** ice crystal shape. Calculated for 30° solar zenith angle, 90° solar azimuth angle, solid columns, 11–13 km cloud height, surface albedo for water and 20 µm effective radius. The benchmark case represents the one-to-one line.

Fig. 9b, it can also be seen that they are quite similar at most detected scattering angles with the exception of the halo region and below 20 °. Since the differences between the scattering phase functions, calculated for different r_{eff}, appear mostly in the forward and backward scattering range but not in the captured scattering angle range, this explains the small variation found in the sensitivity study.

However, the contrast in the scattering intensity between 22° and the surrounding minima for the three r_{eff} in Fig. 9b is large. Thus, in the special case of solid columns as well as other hexagonal shapes (not shown), it will be possible to estimate r_{eff} from the angular sampled spectral radiance data. Unfortunately, those regions of the scattering phase function were covered only twice during this study: on 18 April 2011 (with rough aggregates as the predominant ice crystal shape) and on 23 April 2011 (highly inhomogeneous cirrus). But even in these two cases, the r_{eff} cannot be retrieved: rough aggregates do not produce the 22° halo, and the cloud inhomogeneities on 23 April caused radiance fluctuations that exceed the intensity of the 22° halo. Thus, the retrieval of the r_{eff} from the angular measurements of the spectral radiance data will be part of future investigations.

Furthermore, it was found that there is no significant dependence of the retrieved τ_{ci} on cloud height. The differences

for all four cases are below 1 %. Only on 18 April 2011, the difference was slightly larger with an underestimation of less than 1 %. Therefore, possible uncertainties of the retrieved τ_{ci} due to the cloud height can be neglected. This is also reproducible when looking at the retrieval curves in Fig. 15c, which are congruent. The first variation of the absolute value of τ_{ci} occurs at the third digit behind the decimal point.

The final parameter for which the sensitivity of the retrieval algorithm was tested is the ice crystal shape. As seen in Table 2, the differences show values up to almost 90 % in the measured cirrus fields. The retrieved τ_{ci} in Fig. 15d as well as the scattering phase functions in Fig. 9a confirm this statement. Compared to the other parameters, the retrieval curves show larger differences to each other. This is due to the scattering phase functions, which are quite different to each other for the scattering angle range, which was captured by the four measurement cases. In Fig. 15d the differences between the curves increase with increasing τ_{ci}. By using plates or rough aggregates instead of solid columns, τ_{ci} will be underestimated in both cases. The average of τ_{ci} is larger by up to 0.2. Compared to the average values of the detected τ_{ci} this is not negligible. Therefore, the ice crystal shape is important to accurately retrieve the cirrus optical thickness from ground-based spectral radiance measurements.

6 Summary and conclusions

Downward solar radiance fields were measured with high spatial, spectral and temporal resolution using a hyperspectral imaging spectrometer (AisaEAGLE). The procedure of data evaluation (dark current correction, smear correction) is described at the beginning of this paper. It is shown that the dark current and smear correction must be taken into account for every measurement (calibration included). During the calibration procedure, the entire spectral range (100–1300 nm) must be used for an accurate smear correction.

The cirrus optical thickness (τ_{ci}) is retrieved from the spectral radiance measurements. On the basis of four measurement cases collected during the CARRIBA project in 2011 on Barbados, the feasibility of retrieving cirrus optical thickness at high spatial resolution and characterising the cirrus heterogeneity was demonstrated. The cirrus observed on 16 and 18 April 2011 was quite homogeneous with mean τ_{ci} of 0.28 and 0.20 and coefficients of variation of 0.09 and 0.03. On 9 and 23 April 2011 rather inhomogeneous cirrus with mean τ_{ci} of 0.41 and 0.05 and coefficients of variation of 0.17 and 0.04 was observed.

The sensitivity of the retrieval method was characterised by varying the model input parameters such as the surface albedo, the effective radius, the cloud height and the ice crystal shape. Significant sensitivities of the retrieval method have been found with respect to the surface albedo and the ice crystal shape with up to 30 % and 90 % differences, respectively. The sensitivity of the retrieved cirrus optical thickness with respect to the effective radius ($\leq$ 5%) and the cloud height ($\leq$ 0.5%) is rather small and can be neglected. This indicates that accurate knowledge of the surface albedo and ice crystal shape is required to retrieve a reliable cirrus optical thickness with AisaEAGLE. However, the determination of the ice crystal shape is complicated without in situ measurements inside the cirrus. Due to the fact that AisaEAGLE is able to measure radiance as a function of a wide range of scattering angles, it may provide the opportunity to derive information about the scattering phase function from the radiance measurements. A preliminary estimate of ice crystal shape can be obtained by comparing the directional radiance measured by AisaEAGLE to simulation and analysing the all-sky images. It seems possible to distinguish between hexagonal ice crystals that produce a typical 22° halo and irregular ice crystals that do not. The shape retrieval might be limited to a narrow range of scattering angles which might not cover the halo in some cases. In future studies the detected scattering angle range will be increased, using a scanning version of the AisaEAGLE. The results will then be implemented in the retrieval algorithm. The additional angular information might allow developing a cirrus retrieval technique independent of assumptions about the ice crystal shape.

To adjust the measurement setup for this purpose, the best way to operate AisaEAGLE in a ground-based application is to adjust the sensor line in the azimuthal direction of the Sun, with the clouds heading perpendicularly across the sensor line. Performing the measurements like this, the maximum possible range of the scattering phase function as well as the maximum possible range of the cloud field can be detected without a spatial distortion of the cloud shape.

Acknowledgements. We are grateful for funding of project SI 1534/3-1 and WE 1900/18-1 by the German Research Foundation (Deutsche Forschungsgemeinschaft, DFG) within the framework of CARRIBA. The authors thank the Institute for Tropospheric Research, Leipzig, particularly Holger Siebert, and the Max Planck Institute for Meteorology, Hamburg, for organising the campaign and the logistic support at BCO.

Edited by: S. Schmidt

References

Bierwirth, E., Ehrlich, A., Wendisch, M., Gayet, J.-F., Gourbeyre, C., Dupuy, R., Herber, A., Neuber, R., and Lampert, A.: Optical thickness and effective radius of Arctic boundary-layer clouds retrieved from airborne nadir and imaging spectrometry, Atmos. Meas. Tech., 6, 1189–1200, doi:10.5194/amt-6-1189-2013, 2013.

Carlin, B., Fu, Q., Lohmann, U., Mace, G. G., Sassen, K., and Comstock, J. M.: High-cloud horizontal inhomogeneity and solar albedo bias, J. Climate, 15, 2321–2339, 2002.

DellEndice, F., Nieke, J., Koetz, B., Schaepman, M. E., and Itten, K.: Improving radiometry of imaging spectrometers by using programmable spectral regions of interest, ISPRS J. Photogramm., 64, 632–639, doi:10.1016/j.isprsjprs.2009.05.007, 2009.

Dobbie, S. and Jonas, P.: Radiative influences on the structure and lifetime of cirrus clouds, Q. J. Roy. Meteorol. Soc., 127, 2663–2682, 2001.

Eichler, H., Ehrlich, A., Wendisch, M., Mioche, G., Gayet, J.-F., Wirth, M., Emde, C., and Minikin, A.: Influence of ice crystal shape on retrieval of cirrus optical thickness and effective radius: A case study, J. Geophys. Res., 114, D19203, doi:10.1029/2009JD012215, 2009.

Feister, U. and Grewe, R.: Spectral albedo measurements in the UV and visible region over different types of surfaces, Photocem. Photobiol., 62, 736–744, doi:10.1111/j.1751-1097.1995.tb08723.x, 1995.

Garrett, T. J., Gerber, H., Baumgardner, D. G., Twohy, C. H., and Weinstock, E. M.: Small, highly reflective ice crystals in low-latitude cirrus, Geophys. Res. Lett., 30, 2132, doi:10.1029/2003GL018153, 2003.

Hanus, J., Malenovsky, Z., Homolova, L., Veroslav, K., Petr, L., and Pavel, C.: Potentials of the VNIR Airborne hyperspectral system AISA Eagle, in: Symposium GIS Ostrava, (CZ), 2008.

Liu, H.-C., Wang, P., and Schlesinger, R.: A numerical study of cirrus clouds. Part II: Effects of ambient temperature, stability, radiation, ice microphysics, and microdynamics on cirrus evolution, J. Atmos. Sci., 60, 1097–1119, 2003.

Marshak, A., Davis, A., Wiscombe, W., and Cahalan, R. F.: Radiative smoothing in fractal clouds, J. Geophys. Res., 100, 26247–26261, 1995.

Marsham, J. and Dobbie, S.: The effects of wind shear on cirrus: A large-eddy model and radar case-study, Q. J. Roy. Meteorol. Soc., 131, 2937–2955, 2003.

Mayer, B. and Kylling, A.: Technical note: The libRadtran software package for radiative transfer calculations – description and examples of use, Atmos. Chem. Phys., 5, 1855–1877, doi:10.5194/acp-5-1855-2005, 2005.

McFarlane, S. A. and Marchand, R. T.: Analysis of ice crystal habits derived from MISR and MODIS observations over the ARM Southern Great Plains site, J. Geophys. Res., 113, D07209,doi:10.1029/2007JD009191, 2008.

Oreopoulos, L., Marshak, A., Cahalan, R. F., and Wen, G. Y.: Cloud three-dimensional effects evidenced in Landsat spatial power spectra and autocorrelation functions, J. Geophys. Res., 105, 14777–14788, 2000.

Schmidt, K. S., Pilewskie, P., Platnick, S., Wind, G., Yang, P., and Wendisch, M.: Comparing irradiance fields derived from Moderate Resolution Imaging Spectroradiometer airborne simulator cirrus cloud retrievals with solar spectral flux radiometer measurements, J. Geophys. Res., 112, D24206, doi:10.1029/2007JD008711, 2007.

Shettle, E.: Models of aerosols, clouds and precipitation for atmospheric propagation studies, in: Atmospheric propagation in the uv, visible, ir and mm-region and related system aspects, in: AGARD Conference Proceedings, 454, 1989.

Siebert, H., Bethke, J., Bierwirth, E., Conrath, T., Dieckmann, K., Ditas, F., Ehrlich, A., Farrell, D., Hartmann, S., Izaguirre, M. A., Katzwinkel, J., Nuijens, L., Roberts, G., Schäfer, M., Shaw, R. A., Schmeissner, T., Serikov, I., Stevens, B., Stratmann, F., Wehner, B., Wendisch, M., Werner, F., and Wex, H.: The fine-scale structure of the trade wind cumuli over Barbados – an introduction to the CARRIBA project, Atmos. Chem. Phys. Discuss., 12, 28609–28660, doi:10.5194/acpd-12-28609-2012, 2012.

Varnai, T. and Marshak, A.: Statistical analysis of the uncertainties in cloud optical depth retrievals caused by three-dimensional radiative effects, J. Atmos. Sci., 58, 1540–1548, 2001.

Wendisch, M., Pilewskie, P., Jäkel, E., Schmidt, S., Pommier, J., Howard, S., Jonsson, H. H., Guan, H., Schröder, M., and Mayer, B.: Airborne measurements of areal spectral surface albedo over different sea and land surfaces, J. Geophys. Res., 109, D08203, doi:10.1029/2003JD004392, 2004.

Wendisch, M., Pilewskie, P., Pommier, J., Howard, S., Yang, P., Heymsfield, A. J., Schmitt, C. G., Baumgardner, D., and Mayer, B.: Impact of cirrus crystal shape on solar spectral irradiance: A case study for subtropical cirrus, J. Geophys. Res., 110, D03202, doi:10.1029/2004JD005294, 2005.

Wendisch, M., Yang, P., and Pilewskie, P.: Effects of ice crystal habit on thermal infrared radiative properties and forcing of cirrus, J. Geophys. Res., 112, D08201, doi:10.1029/2006JD007899, 2007.

Werner, F., Ditas, F., Siebert, H., Wehner, B., Pilewskie, P., and Wendisch, M.: Twomey effect and susceptibility of maritime trade wind cumuli, J. Geophys. Res., in review, 2013a.

Werner, F., Siebert, H., Pilewskie, P., Schmeissner, T., Shaw, R. A., and Wendisch, M.: New airborne retrieval approach for trade wind cumulus properties under overlying cirrus, J. Geophys. Res., 118, 3634–3649, doi:10.1002/jgrd.50334, 2013b.

Yang, P., Liou, K. N., Wyser, K., and Mitchell, D.: Parameterization of the scattering and absorption properties of individual ice crystals, J. Geophys. Res., 105, 4699–4718, 2000.